Article

Analysis of Cavitation-Induced Unsteady Flow Conditions in Francis Turbines under High-Load Conditions

Haobo Wang [1], Daqing Zhou [1,2,*], An Yu [2] and Junxun Guo [1]

1   College of Water Conservancy and Hydropower Engineering, Hohai University, Nanjing 210098, China; wanghaobo@hhu.edu.cn (H.W.); guojunxun@hhu.edu.cn (J.G.)
2   College of Electrical and Power Engineering, Hohai University, Nanjing 211100, China; yu_an@hhu.edu.cn
*   Correspondence: zhoudaqing@hhu.edu.cn

Abstract: Hydraulic vibrations in Francis turbines caused by cavitation profoundly impact the overall hydraulic performance and operational stability. Therefore, to investigate the influence of cavitation phenomena under high-load conditions, a three-dimensional unsteady numerical simulation is carried out for a Francis turbine with different head operating conditions, which is combined with the SST k-w turbulence model and two-phase flow cavitation model to capture the evolution of cavitation under high-load conditions. Additionally, utilizing entropy production theory, the hydraulic losses of the Francis turbine during cavitation development are assessed. Contrary to the pressure-drop method, the entropy production theory can quantitatively reflect the characteristics of the local hydraulic loss distribution, with a calculated error coefficient τ not exceeding 2%. The specific findings include: the primary sources of energy loss inside the turbine are the airfoil cavitation and cavitation vortex rope, constituting 26% and 71% of the total hydraulic losses, respectively. According to the comparison with model tests, the vapor volume fraction (VVF) inside the draft tube fluctuates periodically under high-load conditions, causing low-frequency pressure pulsation in the turbine's power, flow rate, and other external characteristic parameters at 0.37 Hz, and the runner radial force fluctuates at a frequency of 1.85 Hz.

Keywords: Francis turbine; cavitation; numerical simulation; entropy production; vapor volume fraction fluctuation

1. Introduction

Under the new energy development strategy, hydroelectric power generation, as a key link in the regulation of electricity, has become an important direction in the frontier of energy technology development. Francis turbines, famous for their wide operating head range and robust stability across various load conditions, find extensive application in large-capacity hydropower plants. However, prolonged operation of the turbine under off-design conditions makes it susceptible to cavitation [1–3], which is mainly manifested as airfoil cavitation extending upward from the blade root and the cavitation vortex rope [4,5] phenomenon at the draft tube. Hence, investigating the evolution of cavitation in Francis turbines under various operating conditions and assessing the impact of cavitation development on the stability of the internal flow field have emerged as prominent areas of contemporary research.

Owing to the relative instability and difficulty of observation during the inception and development of cavitation, scholars both domestically and internationally have primarily used model experiments and numerical simulation methods to carry out relevant research, which focuses on the distribution of the flow field and pressure fluctuation inside the hydraulic turbine under various cavitation number conditions. With model experiments, Jain et al. [6] studied the cavitation performance of pumps as turbines (PATs), observing varying degrees of cavitation development inside the runner and draft tube. A reversible pump turbine's cavitation characteristics were analyzed under pumping conditions by

Tao et al. [7], who summarized the intrinsic relationship between pressure and the bubble volume of the airfoil cavitation and divided it into the best critical cavitation range (BICR) and the best inception cavitation range (BCCR) under different load conditions. Liu et al. [8], from the perspective of the unit under cavitation conditions, found hydrodynamic disturbances and additional thrust fluctuations, which existed at the tail edge of the blades. Feng et al. [9] used the MF-DFA method to solve the problem of difficulty to identify the signal extraction of the cavitation stage of an axial-flow paddle turbine, which provided a new direction for the discrimination of different cavitation development stages of a hydraulic turbine. Research about the Francis turbine under a low head was conducted by Gohil et al. [10], revealing the pressure and amplitude phenomena of the turbine under cavitation. To explore the influences of cavitation on the hump region, Li et al. [11] employed a hybrid approach involving numerical simulations and experiments, revealing characteristic frequencies arising from unsteady flow regimes in the pump turbine. Zhu et al.'s study [12] examined the reversible pump turbines' hydraulic performance under pump mode and discovered that when cavitation develops at the blades, the axial force is brought in progressively.

Currently, to mitigate the impact of cavitation on hydraulic turbines, most studies have achieved significant results through the optimization of the turbine structure, thereby enhancing the cavitation performance of the turbine. By modifying the runner's geometric characteristics using a multi-objective optimization technique, Hu et al. [13] enhanced the turbine's cavitation performance and hydraulic efficiency under part-load conditions. Yu et al. [14] studied the energy characteristics of the pump turbine, analyzing the hydraulic losses of different internal structures quantitatively under various load conditions. Pang et al. [15] summarized the variations in the energy characteristics of the vortex rope's evolution and examined the hydraulic characteristics of the pump turbine. Abu Shahzer et al. [16] investigated the pump turbine operating at different cavitation numbers and proposed a method to effectively suppress the generation of the vortex rope. By installing a fin structure and utilizing air admission, Zhu et al. [17] were able to decrease the amplitude of pressure fluctuations and improve the vortex rope's form distribution. Zhou et al. [18] proposed a method to change the inclination angle of the straight conical section, which can destroy the strong swirl flow inside the draft tube, improving the overall stability of the Francis turbine effectively. Using large-eddy simulations, Altimemy et al. [19] investigated the suppression of the vortex rope phenomenon with varying volumes of water injections, concluding that a volume of water injections over 4% can alleviate pressure surges and has less of an effect on the Francis turbine's operational stability.

In conclusion, the majority of recent research has predominantly focused on the internal field analysis of cavitation within the turbine. Few studies reveal the connection between the evolution of cavitation and the variation of external characteristic parameters, particularly under high-load conditions. Thus, a multiphase flow numerical simulation is carried out for Francis turbines under various load conditions. Utilizing entropy production theory, we analyze the distribution of hydraulic losses in the internal flow field of the turbine during cavitation, uncovering the impact of changes in the vortex rope volume inside the draft tube on external parameters. This paper is structured as follows: the first section introduces the mathematical model used in this study; the subsequent section presents the computational model and relevant settings for multiphase flow simulation; the third section explores hydraulic losses at each structure using entropy production theory; and the final section reveals the hydraulic disturbances caused by changes in the volume of vortex ropes inside the draft tube.

2. Mathematical Methods

2.1. Governing Equations

In this paper, it is assumed that the fluid is incompressible and at a constant temperature in the numerical calculation, so the solution of the energy equation is not considered. In addition, the choice of turbulence model is particularly important in the calculation

accuracy of the wall function. At present, from the multiphase flow numerical studies that have been carried out by different scholars, the SST *k-w* turbulence model has a higher accuracy in multiphase flow calculations [20,21], and the form of vapor cores is more in compliance with the experimental results.

2.2. Cavitation Model

The cavitation model used in the multiphase flow calculations in this paper is the Zwart–Gerber–Belamri model [22], defined through the following equation:

$$m^+ = C_{vap} \frac{3\alpha_{nuc}(1-\alpha_v)\rho_v}{R_B} \sqrt{\frac{2}{3} \frac{\max(p_v - p, 0)}{\rho_l}}, p \leq p_v \tag{1}$$

$$m^- = C_{cond} \frac{3\alpha_v \rho_v}{R_B} \sqrt{\frac{2}{3} \frac{\max(p - p_v, 0)}{\rho_l}}, p \geq p_v \tag{2}$$

where C_{vap} and C_{cond} represent the evaporation coefficient and condensation coefficient, respectively; α_{nuc} is the volume fraction of the nucleation location; R_B is the radius of the bubble; and p_v represents the saturated vapor pressure.

The two-phase flow calculations for hydraulic turbines are mainly concerned with the mass transfer [23] between the water and vapor phases, so the density and dynamic viscosity of the mixed phase can be obtained from the following equations:

$$\rho_m = \alpha_l \rho_l + (1 - \alpha_l)\rho_v \tag{3}$$

$$\mu_m = \alpha_l \mu_l + (1 - \alpha_l)\mu_v \tag{4}$$

The volume integral and mass transfer equations for each phase can be obtained from the following equations:

$$\alpha_n = \frac{V_n}{V} \tag{5}$$

$$\frac{\partial \rho_v \alpha_v}{\partial t} + \frac{\partial \rho_v \alpha_v u_j}{\partial x_j} = m^+ - m^- \tag{6}$$

where α_n is the volume integral of vapor; m^+ is the evaporating phase, representing the mass of vapor gained by the evaporation process; and m^- is the condensing phase, representing the mass of vapor lost by the condensation process.

2.3. Cavitation Number

In this paper, the cavitation number σ of the turbine operation is varied by controlling the outlet pressure of the draft tube, where the cavitation number σ is defined by the following equation:

$$\sigma = \frac{P_{out} - P_v}{\rho g H} - \frac{H_s}{H} \tag{7}$$

where P_{out} is the outlet pressure of the draft tube; H_s is the static suction of the turbine; H is the turbine operating head; ρ is the fluid density; and g is the acceleration due to gravity.

2.4. Entropy Production Theory

Employing the RANS (Reynolds averaged Navier–Stokes) time-averaged method, the viscous entropy production S_T can be divided into two parts. $\dot{S}_{\overline{D}}$ is the direct dissipation phase, which is caused by time-averaged velocities in the flow; $\dot{S}_{D'}$ represents the turbulent dissipation phase, which is caused by fluctuating velocity in the flow.

$$\dot{S}_T = \dot{S}_{\overline{D}} + \dot{S}_{D'} \tag{8}$$

$$\dot{S_{\overline{D}}} = \frac{\mu}{T}\left[2\left(\left(\frac{\partial\overline{u}}{\partial x}\right)^2 + \left(\frac{\partial\overline{v}}{\partial y}\right)^2 + \left(\frac{\partial\overline{w}}{\partial z}\right)^2\right) + \left(\frac{\partial\overline{u}}{\partial y} + \frac{\partial\overline{v}}{\partial x}\right)^2 + \left(\frac{\partial\overline{u}}{\partial z} + \frac{\partial\overline{w}}{\partial x}\right)^2 + \left(\frac{\partial\overline{v}}{\partial z} + \frac{\partial\overline{w}}{\partial y}\right)^2\right] \tag{9}$$

$$\dot{S_{D'}} = \frac{\mu_{eff}}{\overline{T}}\left[2\left(\left(\frac{\partial u'}{\partial x}\right)^2 + \left(\frac{\partial v'}{\partial y}\right)^2 + \left(\frac{\partial w'}{\partial z}\right)^2\right) + \left(\frac{\partial u'}{\partial y} + \frac{\partial v'}{\partial x}\right)^2 + \left(\frac{\partial u'}{\partial z} + \frac{\partial w'}{\partial x}\right)^2 + \left(\frac{\partial v'}{\partial z} + \frac{\partial w'}{\partial y}\right)^2\right] \tag{10}$$

$$\dot{S_{D'}} = \beta\frac{\rho\omega k}{T} \tag{11}$$

$$\mu_{eff} = \mu + \mu_t \tag{12}$$

where β is 0.09; k is the turbulent kinetic energy; ω is the turbulent dissipation rate; T is the temperature; and μ_t is the eddy viscosity.

In addition, to obtain a more accurate distribution of the wall entropy production, a wall energy dissipation model proposed by Duan et al. [24] is applied. It can be obtained by Equation (13):

$$S_w = \int_A \frac{\tau \cdot v_p}{T}dA \tag{13}$$

where τ is the wall shear stress; v_p is the velocity in the center of the first grid layer near the wall.

Thus, the total entropy production rate (TEPR) is the sum of the three types of entropy production rate: direct entropy production rate, indirect entropy production rate, and wall entropy production rate. The total entropy production of the computational domain is obtained through Equation (14):

$$S = \int_V \dot{S_{\overline{D}}}dV + \int_V \dot{S_{D'}}dV + S_w \tag{14}$$

3. Numerical Calculation Model

3.1. Calculation Model

The detailed operating parameters of the turbine are shown in Table 1. The subject of this paper is a prototype Francis turbine in a hydropower station [25], as shown in Figure 1, which includes a spiral casing (SC), guide vanes (GV), stay vanes (SV), runner (RU), and draft tube (DT). In addition, to obtain more accurate hydraulic forces of the turbine from different directions, we take microscale structures such as the upper clearance and lower clearance into account.
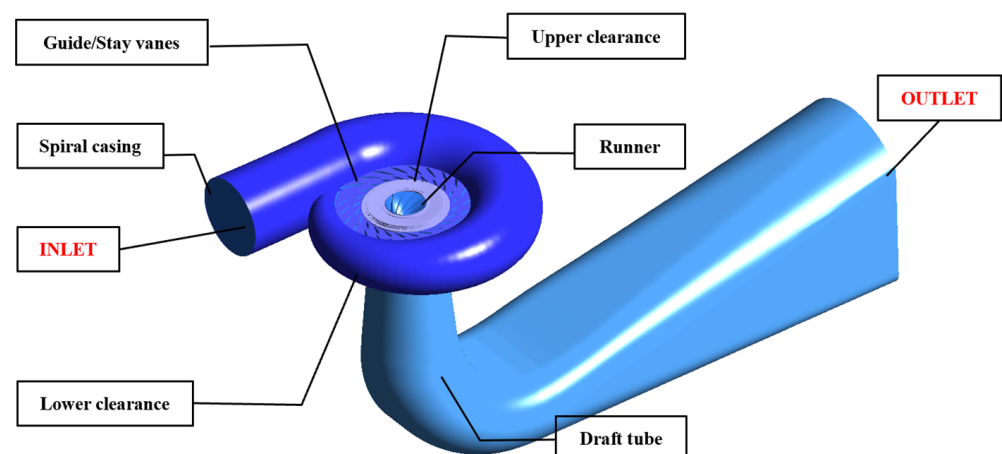
Figure 1. Francis turbine three-dimensional model.

Table 1. Operating parameters of the Francis turbine.

Parameter	Value
Maximum head H_{max} (m)	243.1
Minimum head H_{min} (m)	163.9
Rated head H_r (m)	202
Runner inlet diameter D_1 (m)	8.47
Number of runner blades N_r	15
Rated rotation speed n (rpm)	111.1

3.2. Computational Domain Discretization

A specific number of meshes and a reasonable distribution scheme are essential. Given the intricate geometrical structure of the spiral casing and guide vanes, unstructured tetrahedral meshing using ANSYS-ICEM 2021R1 software is employed. The remaining turbine components are meshed with a hexahedral structured mesh. To achieve higher accuracy in wall function solving, additional refinement of the boundary-layer mesh is applied in regions of elevated flow intensity. Balancing considerations such as computing time and resources, the y+ value on the wall surface is constrained to be less than 30.

3.3. Mesh Independent Verification

As shown in Figure 2, by conducting numerical calculations for both multiphase and single-phase flows under the rated head's optimal condition and comparing the changes in the external characteristic parameters across six grid number allocation schemes (3.92 million, 4.83 million, 5.91 million, 6.76 million, 7.69 million, and 8.91 million), it can be observed that the unit efficiency and moment parameters exhibit a gentler increase with the grid number reaching 8 million, finally converging to stability, which proves that the change in the number of grids has less influence on the calculation results. Therefore, the total number of 8.91 million grids is taken as the optimal scheme for the subsequent computational domain discretization, in which the distribution of the number of grids at each part of the unit is shown in Table 2, and the orthogonal quality of the grids of each part of the unit is greater than 0.35, which meets the requirement of computational accuracy in numerical simulation.
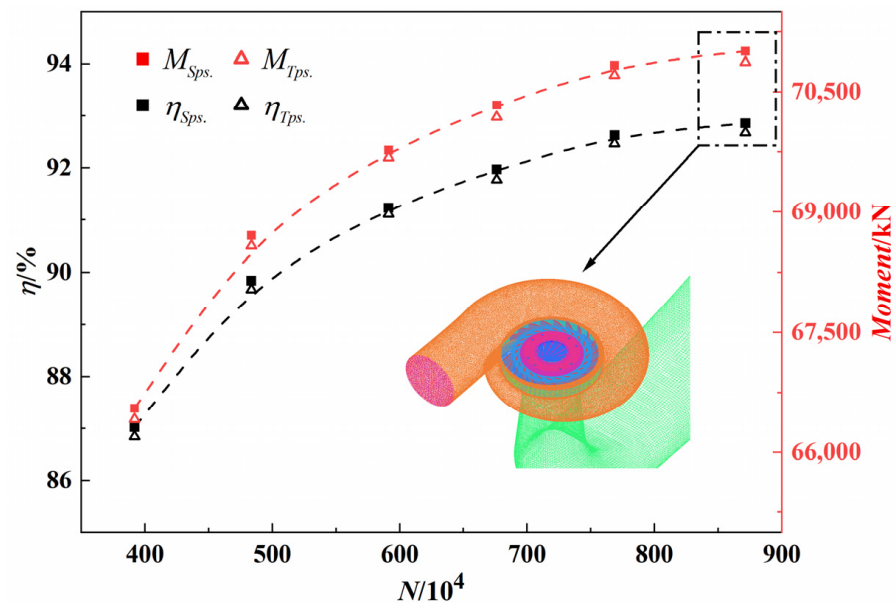
Figure 2. Schematic of grid-independent verification.

Table 2. Distribution of the number of grids.

Part	Mesh Type	Orthogonal Quality	Mesh Number (10^4)
Spiral Casing (SC)	Tetrahedral	0.36	101.9
Upper Clearance	Hexahedral	0.42	151.1
Stay Vanes (SV)	Tetrahedral	0.45	84.6
Guide Vanes (GV)	Tetrahedral	0.48	96.3
Runner (RU)	Hexahedral	0.52	262.9
Lower Clearance	Hexahedral	0.46	89.7
Draft Tube (DT)	Hexahedral	0.56	95.7
Extended Pipes	Hexahedral	0.78	8.9
Total	\	\	891.1

3.4. Boundary Condition Setting

In this study, numerical simulations of multiphase flow in a Francis turbine under various loading conditions are conducted using ANSYS-CFX 2021R1 software. Pressure boundary conditions are adopted at the inlet and outlet to maintain the turbine in different head conditions, with the adjustment of the guide vane opening controlling the turbine output. The second-order backward Euler format is used for the discretization of the time term, and the high-resolution format is used for the discretization of the convective and turbulent term. The RMS (root mean square) convergence criterion is used for each variable in the calculations, with the number of convergence iterations set to 20 and the final convergence value set to 10^{-5}. The time step taken in the transient calculations is set to be 4.5×10^{-3}. The no-slip boundary condition is applied in the calculation of the wall surfaces, and GGI is set at the interface of the different grids.

4. Analysis of Calculation Results

4.1. Numerical Accuracy Verification

Figure 3 shows the comparison of the numerical simulation accuracy with the experiment parameter schematic. Based on the calculation results for single-phase flow, we conduct ten load conditions for the comparison of multiphase flow numerical simulation. As shown in the figure, the numerical simulation results of the multiphase flow calculation are more compliant with the trend of the test, as well as the accuracy of the calculations under various conditions to meet the requirements of the calculations. In this paper, we mainly focus on the cavitation of the Francis turbine under high-load conditions; hence, Case 1, Case 2, and Case 3 are selected, and the parameters of the operating conditions are shown in Table 3.
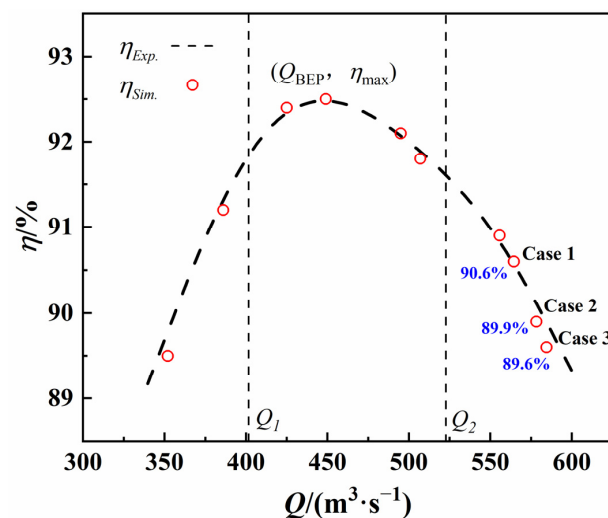
Figure 3. Verification of the accuracy of numerical simulation calculations.

Table 3. Selection of working conditions for calculation.

Case	Head/m	$Q/\text{m}^3 \cdot \text{s}^{-1}$	$\eta/\%$	σ
Case 1	180	564.4	90.6	0.122
Case 2	185	578.2	89.9	0.120
Case 3	190	584.6	89.6	0.119

4.2. Total Hydraulic Loss Distribution of the Turbine

To assess the calculation accuracy of the entropy production theory in comparison to the pressure-drop method, an error coefficient τ in Equation (15) is introduced for evaluation, where h_T represents the head loss coefficient calculated with the pressure-drop method and h_s represents the head loss calculated with the entropy production theory, which can be calculated with Equation (16).

$$\tau = \frac{h_s - h_T}{h_T} \tag{15}$$

$$h_s = \frac{T \cdot S_D}{\rho g Q} \tag{16}$$

where T is the temperature, K; S_D is the total entropy production in the calculation domain, W/K; Q is the actual overflow of the turbine, m^3/s.

As can be seen from Figure 4, the hydraulic loss derived from the pressure-drop method is closer to the entropy production calculation results, with a maximum coefficient of error of 1.75% in Case 1, and with the flow rate increase the error is relatively reduced, with a minimum coefficient of variance of 0.73% in Case 3. The total calculation distributions of both show similarity, but because the entropy production method can quantitatively obtain the specific distribution of hydraulic losses and can estimate the energy loss caused by different hydraulic loss phenomena such as internal flow vortex [26,27], inverse gradient flow, and backflow, it has become an important means of evaluating the hydraulic efficiency of hydraulic machines at present [28,29].
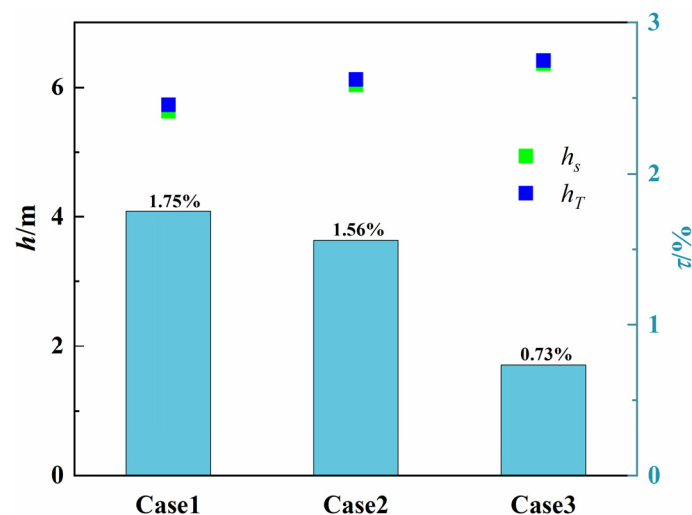
Figure 4. Comparison of the results of pressure-drop method and entropy production.

Figure 5 shows the total internal hydraulic loss of the turbine under different operating conditions and the distribution of head loss at each structure. As the flow rate increases, the total hydraulic loss gradually increases from 5.63 m under Case 1 to 6.37 m under Case 3, of which the percentage of internal hydraulic loss in the draft tube can be up to about 70%, followed by hydraulic loss at the runner, constituting approximately 25%, and the energy loss in the guide vanes and spiral casing is relatively insignificant. From the

distribution of different types of entropy production, the hydraulic loss caused by viscous entropy production S_T accounts for a larger percentage, while the energy loss caused by wall entropy production S_w is relatively lower.
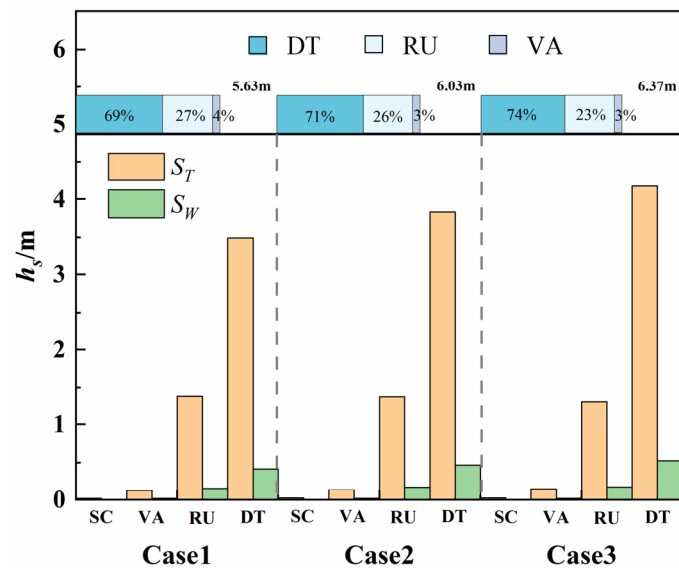
Figure 5. Distribution of hydraulic losses under different operating conditions.

4.3. Analysis of Internal Flow Field

Figure 6 shows the pressure and local entropy production distribution in a cross section of the spiral casing under different working conditions. As the load increases, the fan-shaped low-pressure area at the outlet of the guide vanes improves and gradually shrinks to the runner, and the water flowing into the guide vane from the spiral casing produces a more violent impact phenomenon. Therefore, the more intensive local high-pressure phenomenon can be seen at the head of the guide vanes. Moreover, the local entropy production rate at the guide vanes is gradually increasing; as the entropy production distribution diagram illustrates, the high-entropy-production area is primarily concentrated in the exported region of the guide vanes. Additional factors that contribute to the guide vanes producing a centralized distribution of the local entropy production include the rotor–stator interaction (RSI) between the guide vanes and the runner, as well as the phenomena of vortex and reflux that occur in this area.

Figure 7 illustrates the distribution of the internal flow field at the z = 0 section of the runner under various loading conditions. In high-load conditions, the internal low-pressure region of the runner predominantly resides at the root of the runner blades. As the load increases, this low-pressure area gradually shifts from the leading edge to the trailing edge of the turbine. Additionally, influenced by the local low-pressure region on the suction surface (SS) of the runner, a micro-scale vortex structure forms, as depicted in the total entropy production rate (TEPR) distribution at the runner. The region of high local entropy production is primarily concentrated at the center of the vortex, demonstrating that the entropy production method effectively reflects the local vortex distribution in the internal flow field. Furthermore, according to Figure 7, which depicts the distribution of VVF at the runner's blade under various load conditions, airfoil cavitation begins at the trailing edge and develops along the middle cross section to the blade's leading edge, with the majority of the cavitation's serious area concentrated in the blade pressure surface (PS). The numerical simulation's results agree with Wu et al.'s experimental findings [30]. Under inception cavitation conditions, small cavitation vapor bubbles initially form at the trailing edge of the runner blades and then progress toward the runner's bottom ring.
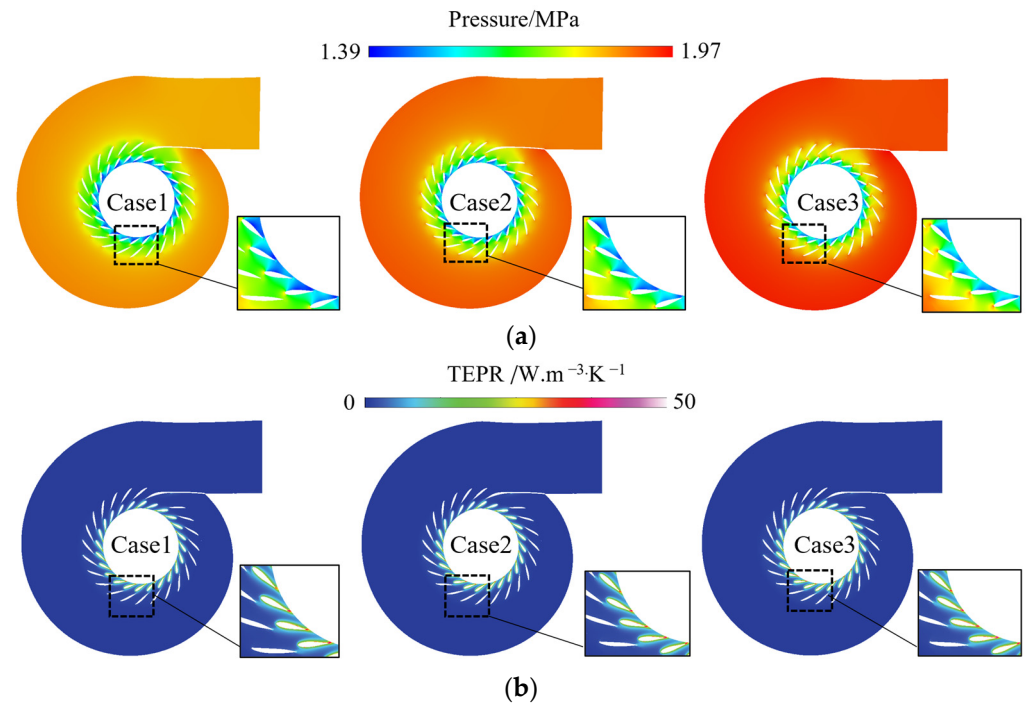
Figure 6. Flow field distribution in spiral casing cross section: (**a**) pressure field in spiral casing; (**b**) TEPR field in spiral casing.
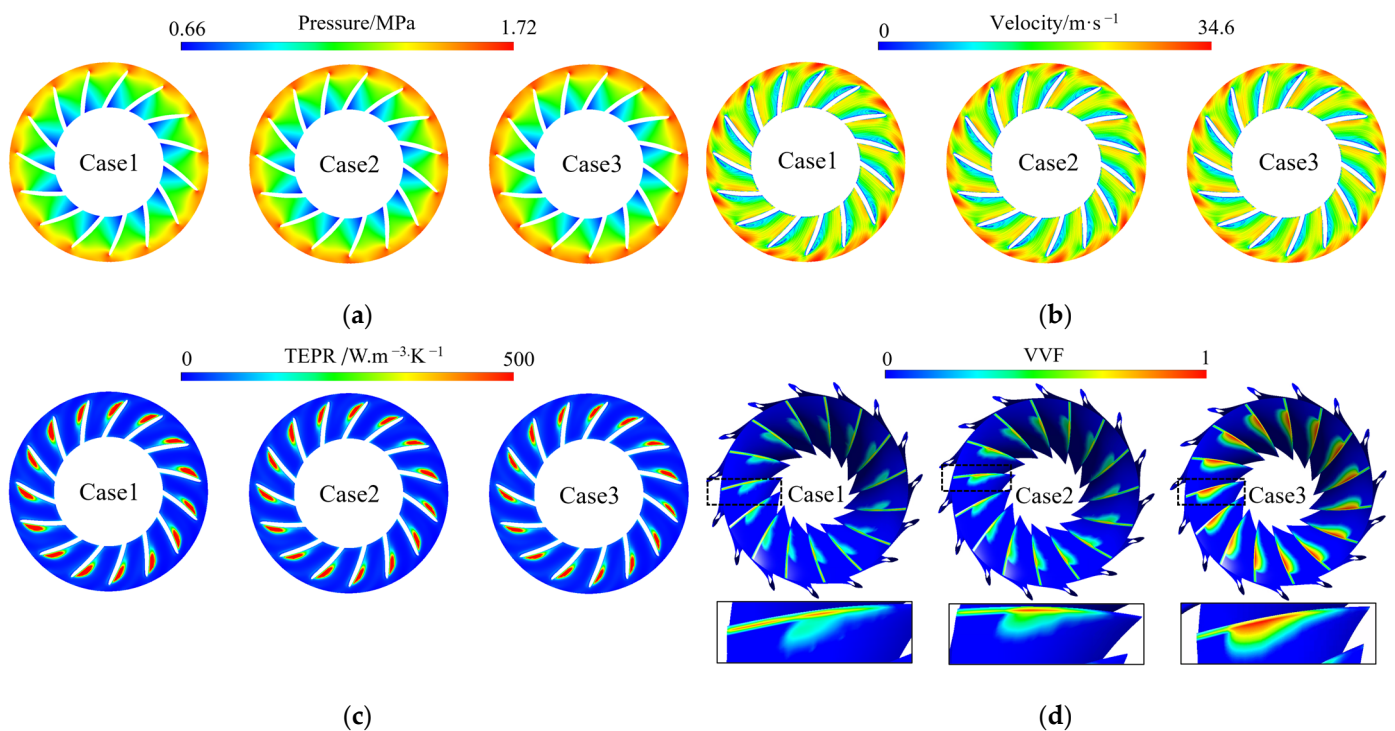
Figure 7. Flow field distribution in runner under different operating conditions: (**a**) pressure field in runner; (**b**) velocity field in runner; (**c**) TEPR field in runner; (**d**) VVF field in runner.

In Figure 8, to obtain insight into the connection between the development of cavitation and energy loss inside the runner, the distribution of the internal flow field at span = 0.3, 0.6, and 0.9 is studied. Furthermore, the subsequent research investigates deeply the effect of airfoil cavitation at the runner's pressure surfaces (PS) and suction surfaces (SS).
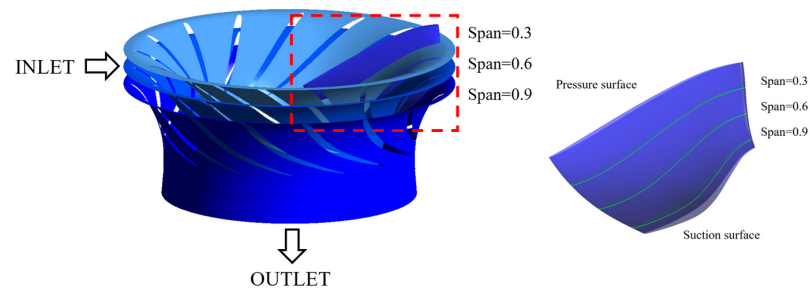
Figure 8. Distribution of different span sections in the runner.

The distribution relationship among pressure, velocity, and the local entropy production rate at the runner's span section under various operating conditions is illustrated in Figure 9. During high-load conditions, it is observed that, under different load conditions, the general distribution of flow field variables across various blade span sections remains consistent. However, a local concentration area is more likely to form near the upper crown of the runner and the bottom ring position [31]. The cavitation distribution diagram of the runner indicates that cavitation phenomena along the runner's trailing edge are inclined to result in a high entropy production distribution. Moreover, the PS and SS exhibit relatively greater instability in pressure and velocity distribution due to backflow, vortex, and other phenomena. This instability leads to a high-pressure distribution, significant velocity fluctuations, and other intricate hydrodynamic vibration phenomena [32].
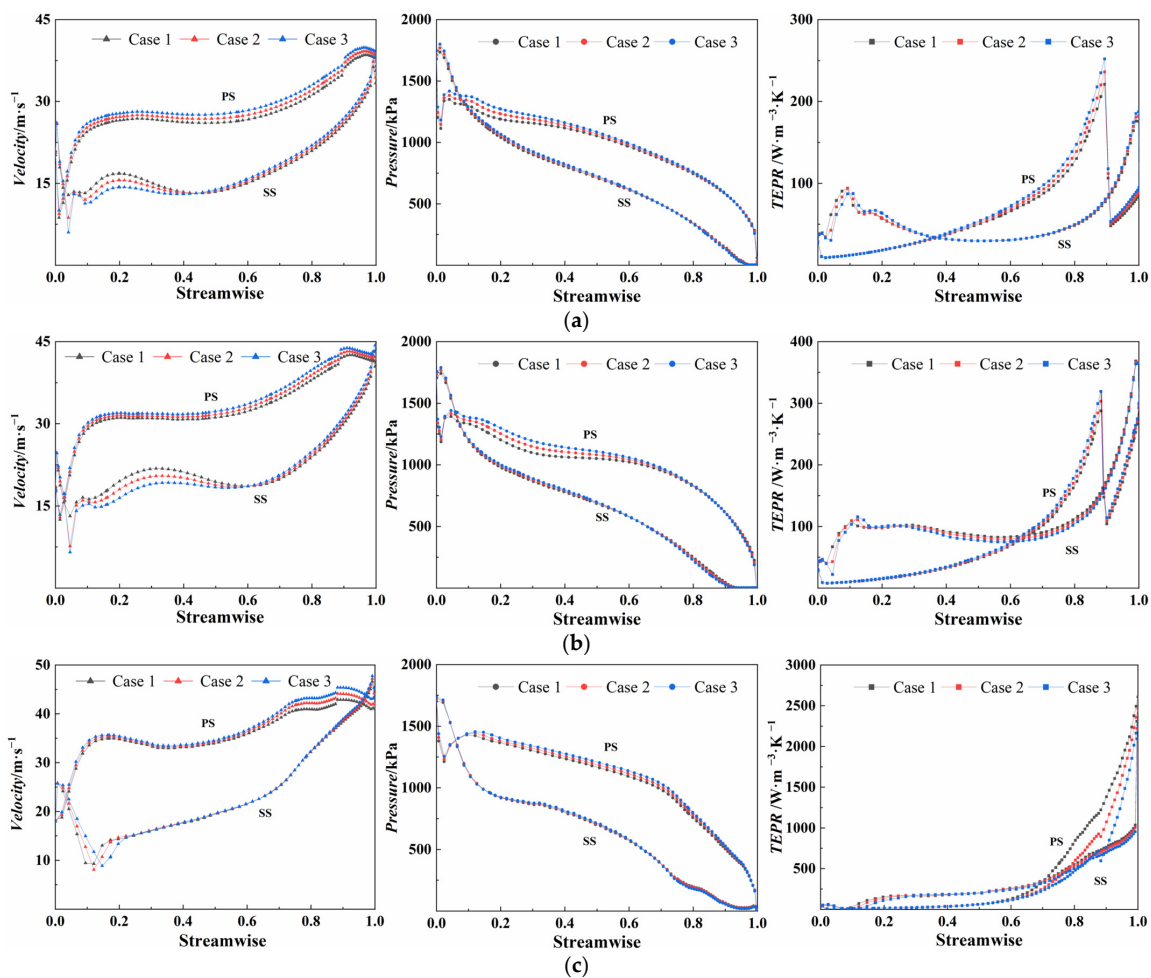
Figure 9. Distribution of flow field on the blade of different span sections: (**a**) span = 0.3; (**b**) span = 0.6; (**c**) span = 0.9.

Figure 10 shows the internal flow field distribution and the shape of the vortex rope inside the draft tube. Under high-load conditions, the vortex rope inside the draft tube exhibits a spindle shape [33,34]. Just as stated in Kumar's paper [35], under rated conditions, the inlet flow at the draft tube is nearly identical to the normal outflow; however, as the flow rate increases, the strong swirl flow is directed contrary to the runner's rotation, and eventually, a cavitation vortex rope shaped like torch forms. In addition, as shown in the black highlighted area of the figure, the motion of the vortex rope has a significant effect on the flow pattern at the inlet inside the draft tube, forming a high-speed zone and a large-scale vortex structure below the vortex rope [36]. As the load increases, the vortex distribution at the outlet of the draft tube is improved; nevertheless, in the red wireframe area of the figure, the vortex ropes are gradually serious and closer to the elbow section in the Case 3 condition, so the energy loss caused by the vortex ropes inside the draft tube will increase. Just as shown by the entropy production distribution, large hydraulic losses [37] are primarily concentrated inside and at the bottom of the cavitation vortex ropes.
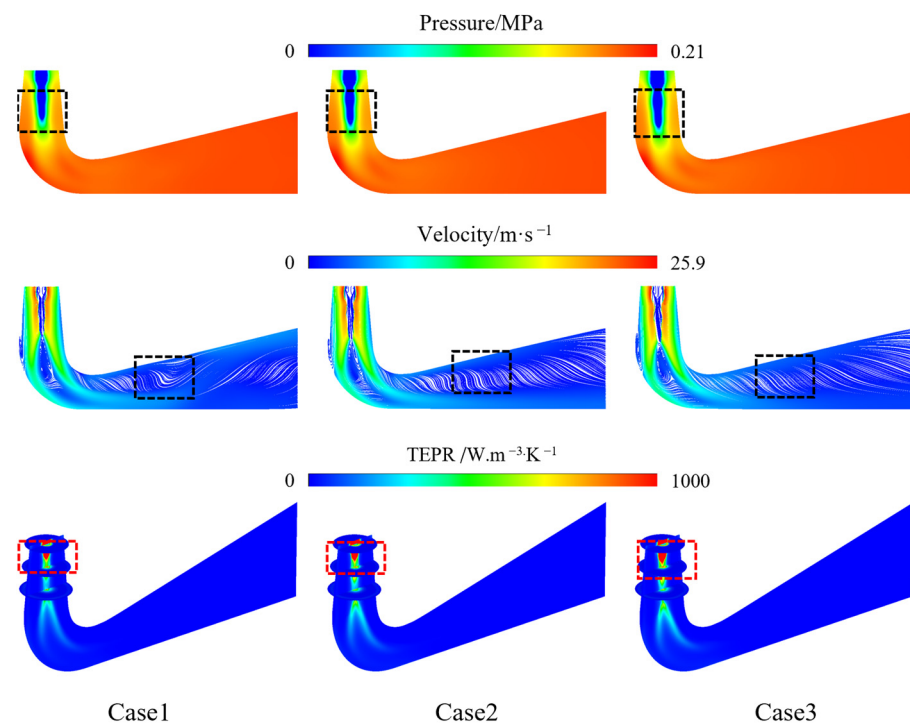
Figure 10. Flow field distribution in draft tube cross section.

4.4. Analysis of Power Fluctuation Factors

The distribution of the vortex rope inside the draft tube under various load conditions is seen in Figure 11. Due to the action of the circumferential velocity component at the runner's outlet [38], the inlet flow of the draft tube can easily transform into an eccentric spiral vortex rope when the flow rate is less than Q_1. With the flow rate increasing, the turbine's operating condition tends to approach the optimal operating condition point. At this point, the draft tube's vortex rope takes on a concentric cylindrical shape, which minimizes the disturbance and influence of the vortex rope motion on the internal flow field, allowing for the generation of higher hydraulic efficiency. However, when the overflows are more than Q_2, the hydraulic turbine operates at high-load conditions when the vortex rope takes on a spindle shape. In addition, the vortex rope's volume change has its fluctuation frequency. If the vortex rope's self-excited frequency approaches the intrinsic frequency of the turbine, it will pose a serious threat to the unit's safety.
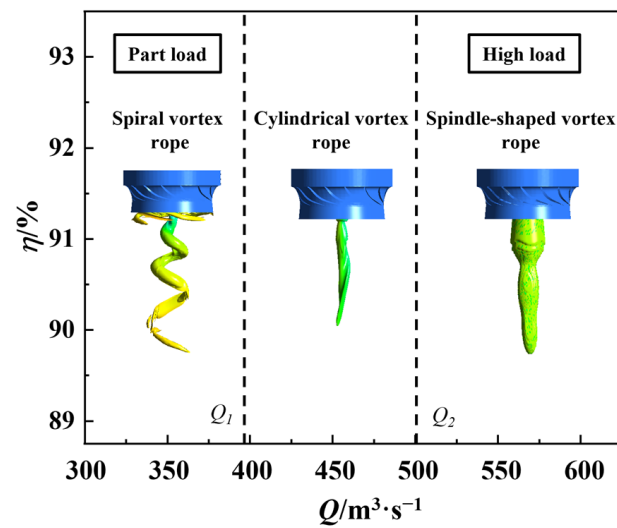
Figure 11. Distribution of different types of vortex ropes in the draft tube.

Figure 12 shows the volumetric change in the vortex rope under Case 2. By comparing and analyzing it with the model test under high-load conditions, the numerical simulation results in this paper are consistent with the trend in the vortex rope shape change in the experimental picture. As can be observed from the graph, the spindle-shaped vortex rope under this condition can be divided into two parts: the upper hammer structure and the lower tail structure, and there is radial contraction and expansion of the upper structure during the operation of the turbine, while the vortex rope also has volumetric oscillations in the axial direction, which makes the turbine's external characteristic parameters also appear to have a periodic fluctuation. Therefore, it is necessary to analyze the effect of the volume change in the spindle vortex rope on the operation of the unit under high-load tconditions.

(a) $t = \dfrac{T}{6}$ (b) $t = \dfrac{2T}{6}$ (c) $t = \dfrac{3T}{6}$
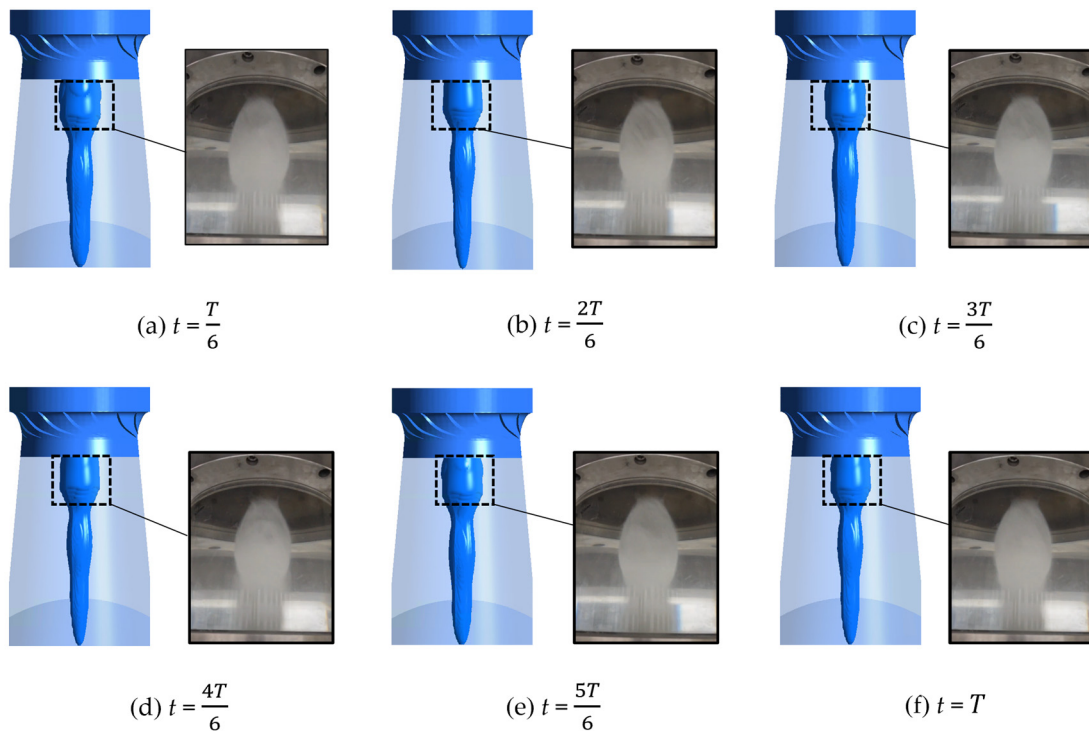
(d) $t = \dfrac{4T}{6}$ (e) $t = \dfrac{5T}{6}$ (f) $t = T$

Figure 12. Schematic of cavitation vortex ropes compared to model tests: (**a**) $t = T/6$; (**b**) $t = 2T/6$; (**c**) $t = 3T/6$; (**d**) $t = 4T/6$; (**e**) $t = 5T/6$; (**f**) $t = T$.

The unit's radial force and external characteristic parameters are displayed in Figure 13. The spindle-shaped vortex rope exhibits a periodic volume change. The relative amplitude changes in the VVF in the $1/6T$ period range is 20.1%, and the amplitude fluctuation frequency of the amplitude is 0.37 Hz. As shown by the fluctuation frequency domain graph, the low frequency also appears similarly in the other external characteristic parameters' frequency domain graphs of the turbine. For instance, the unit flow rate in the vortex rope volume change cycle fluctuation frequency is 0.37 Hz; in the $1/6T$ cycle interval amplitude fluctuation, it is 1.13%, and with the vortex rope volume increase it presents the trend of first decreasing and then increasing. In addition, the unit power parameter also has the same frequency of low-frequency fluctuations and is accompanied by a high-frequency amplitude phenomenon of 5.18 Hz, while the power in the $1/6T$ cycle interval has relative amplitude fluctuations of 1.89%. Therefore, the volume change in& the spindle vortex rope inside the draft tube is influenced by the unit overflow, which in turn affects the hydraulic thrust effect on the runner and indirectly affects the runner by the hydraulic torque effect. As shown in Figure 14, the radial forces in the x and y direction are subject to varying degrees of hydraulic force fluctuations, and the fluctuation frequency of the runner radial force parameter is 1.85 Hz.
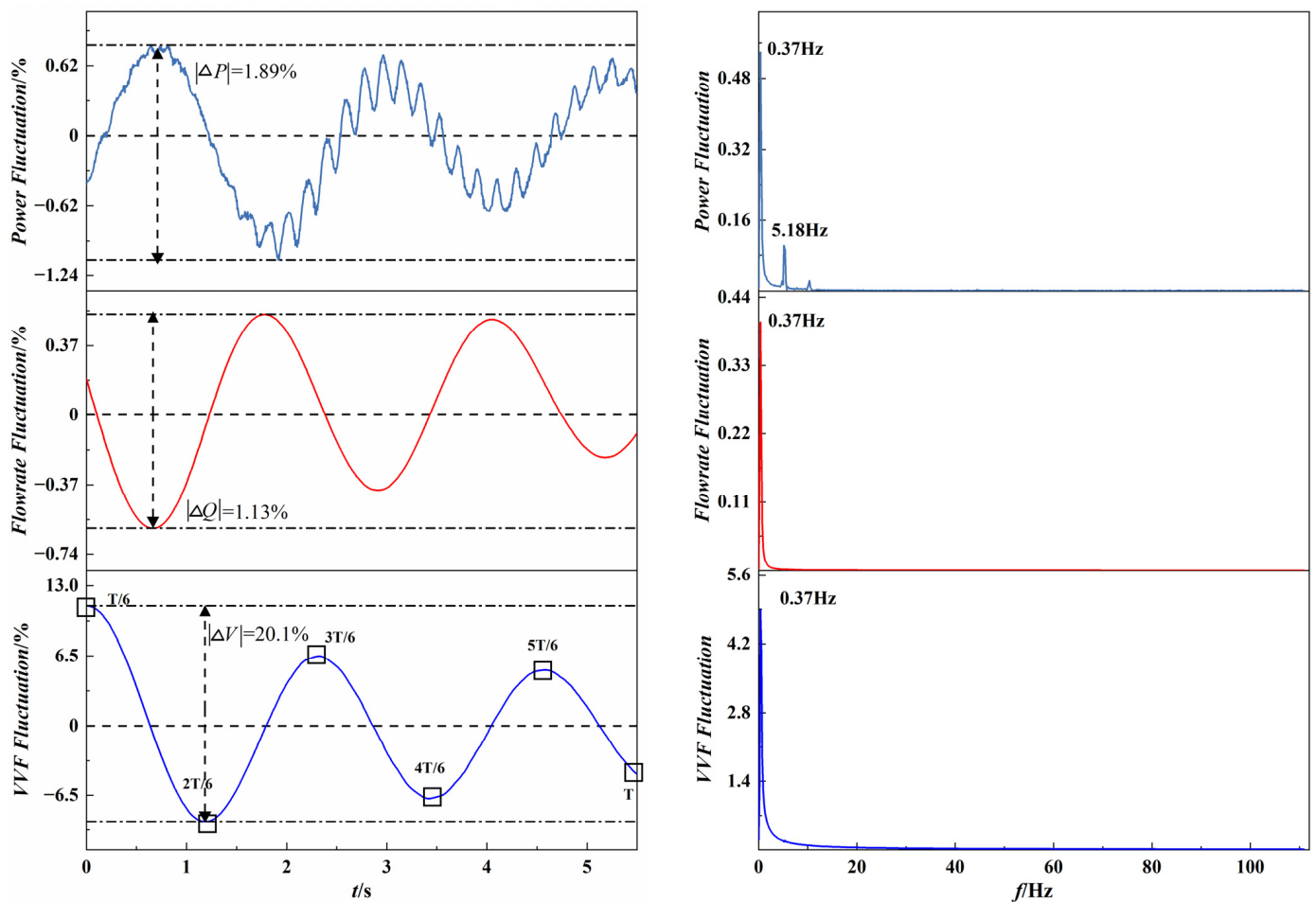
Figure 13. Variation of external characteristic parameters of the turbine.
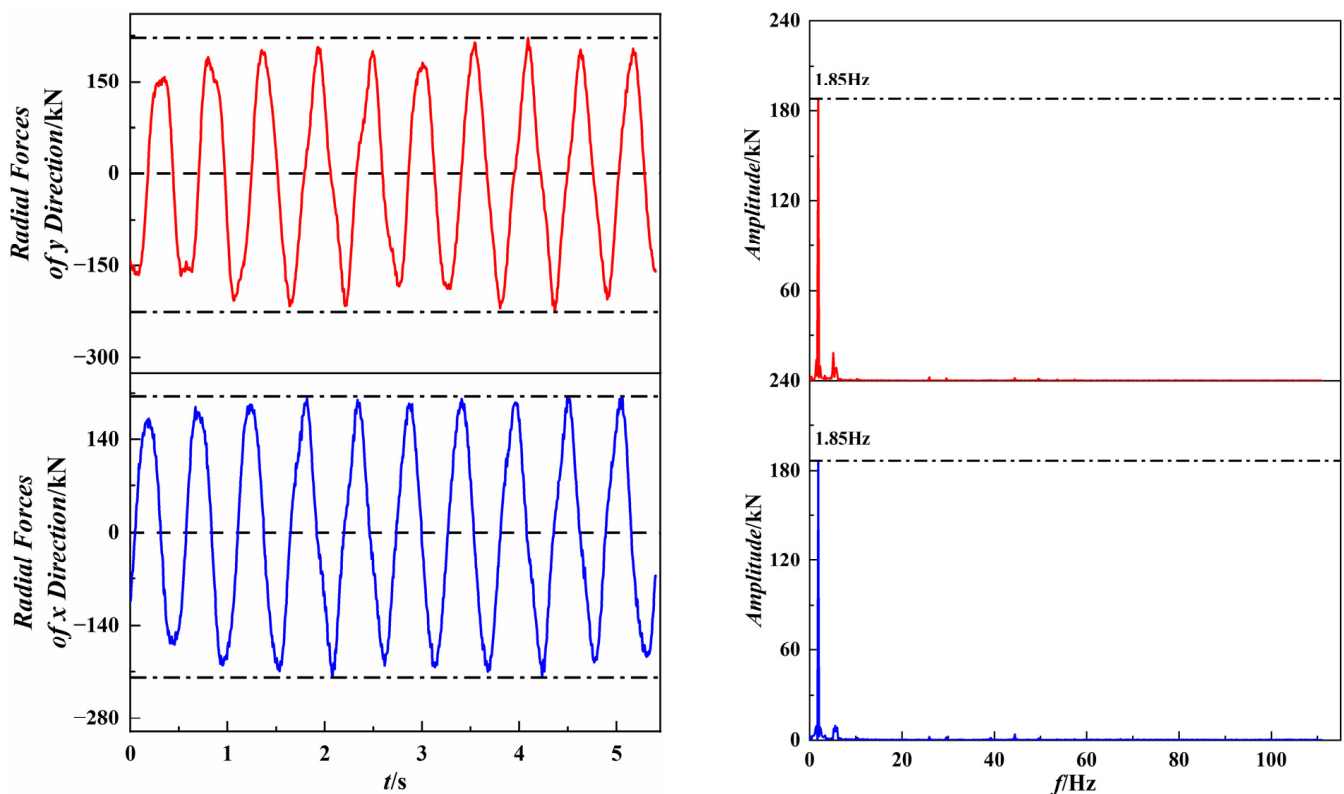
Figure 14. Radial force fluctuation diagram of the runner.

5. Conclusions

We conduct numerical simulations of a Francis turbine for two-phase flow under high-load conditions. The energy losses of the internal flow field are analyzed by applying the entropy production theory; moreover, the effect of the volume change in the spindle vortex rope on the operation of the turbine is revealed. The related research results are as follows:

(1) When evaluating hydraulic losses within the turbine, the entropy production theory is identical to the pressure-drop method, demonstrating a distinct advantage in accurately when characterizing the distribution of hydraulic losses in the localized internal flow field of the turbine.

(2) As the load increases, the hydraulic losses exhibit a climbing trend, predominantly concentrated in the runner and draft tube components, while the hydraulic losses in the guide vane and spiral casing constitute a relatively small proportion. Under Case 3 conditions, the overall hydraulic loss of the unit can reach 6.25 m, with the hydraulic losses inside the draft tube and runner components accounting for 74% and 23% of the total head loss, respectively. The primary contributor to energy loss is viscous entropy production S_T, followed by wall entropy production.

(3) A concentrated distribution of entropy generation might result from varying degrees of cavitation inside the turbine. By analyzing the internal flow field distribution of the unit under three different high-load conditions, the distribution of hydraulic losses is more obvious in different span sections of the runner, and more intense amplitude fluctuations of the variables occur in the SS and the PS of the runner.

(4) The volume change in the spindle vortex rope inside the draft tube will indirectly lead to the power fluctuation phenomenon. In Case 2, the VVF inside the draft tube has a periodic change frequency of 0.37 Hz and causes the same frequency of fluctuation interference in both the flow rate and power parameters, while the runner is subjected to the radial force with a frequency of 1.85 Hz.

This paper investigates the influences of cavitation vortex ropes on Francis turbines under high-load conditions, which can lead to fluctuation to some extent in external characteristic parameters like flow rate and power. In future studies, experiments and numerical simulation related to the technique of suppressing the vortex ropes will be the focused.

Author Contributions: Conceptualization, H.W. and D.Z.; methodology, H.W. and A.Y.; software, H.W.; validation, H.W., D.Z., A.Y. and J.G.; formal analysis, J.G.; resources, D.Z.; data curation, H.W.; writing—original draft preparation, H.W.; writing—review and editing, H.W. and J.G.; supervision, D.Z. and A.Y.; project administration, D.Z.; funding acquisition, D.Z. All authors have read and agreed to the published version of the manuscript.

Data Availability Statement: Data are contained within the article.

Conflicts of Interest: The authors declare no conflicts of interest.

Nomenclature

C_{vap}	evaporation coefficient (-)
C_{cond}	condensation coefficient (-)
α_{nuc}	volume fraction of the nucleation location (-)
R_B	radius of the bubble (m)
p_v	saturated vapor pressure (Pa)
α_v	volume integral of vapor (-)
m^+	evaporating phase (kg·m^{-3}·s)
m^-	condensing phase (kg·m^{-3}·s)
σ	cavitation number (m)
H_s	static suction of the turbine (m)
ρ	fluid density (kg·m^{-3})
g	acceleration due to gravity (m·s^{-2})
$\dot{S}_{\overline{D}}$	direct dissipation phase (W·m^{-3}·K^{-1})
$\dot{S}_{D'}$	turbulent dissipation phase (W·m^{-3}·K^{-1})
k	turbulent kinetic energy (m^2·s^{-2})
ω	turbulent dissipation rate (s^{-1})
T	temperature (K)
μ_t	turbulent viscosity (Pa·s)
τ	wall shear stress (Pa)
S_w	wall entropy production (W·K^{-1})
v_p	velocity in the center of the first grid layer (m·s^{-1})
S_D	total entropy production (W·K^{-1})

References

1. Adhikari, R.C.; Vaz, J.; Wood, D. Cavitation Inception in Crossflow Hydro Turbines. *Energies* **2016**, *9*, 237. [CrossRef]
2. Krzemianowski, Z.; Kaniecki, M. Low-head high specific speed Kaplan turbine for small hydropower—Design, CFD loss analysis and basic, cavitation and runaway investigations: A case study. *Energy Conv. Manag.* **2023**, *276*, 116558. [CrossRef]
3. Zhou, L.; Hang, J.W.; Bai, L.; Krzemianowski, Z.; El-Emam, M.A.; Yasser, E.; Agarwal, R. Application of entropy production theory for energy losses and other investigation in pumps and turbines: A review. *Appl. Energy* **2022**, *318*, 119211. [CrossRef]
4. Dong, W.; Zhenggui, L.; Qing, Z.; Deyou, L.; Wanquan, D.; Lei, J.; Peng, S. Pressure pulsation analysis of runner and draft tube of pump turbine under different working conditions. *IOP Conf. Ser. Earth Environ. Sci.* **2022**, *1037*, 012036.
5. Jošt, D.; Škerlavaj, A.; Lipej, A. Numerical flow simulation and efficiency prediction for axial turbines by advanced turbulence models. *IOP Conf. Ser. Earth Environ. Sci.* **2012**, *15*, 062016. [CrossRef]
6. Jain, S.V.; Patel, N.K.; Patel, R.N. Experimental Investigations of Cavitation Characteristics of Pump Running in Turbine Mode. *J. Energy Eng.* **2017**, *143*, 04016034. [CrossRef]
7. Tao, R.; Xiao, R.; Wang, F.; Liu, W. Cavitation behavior study in the pump mode of a reversible pump-turbine. *Renew. Energy* **2018**, *125*, 655–667. [CrossRef]

8.   Liu, Y.Y.; Gong, J.G.; An, K.; Wang, L.Q. Cavitation Characteristics and Hydrodynamic Radial Forces of a Reversible Pump-Turbine at Pump Mode. *J. Energy Eng.* **2020**, *146*, 04020066. [CrossRef]

9.   Feng, J.; Men, Y.; Zhu, G.; Li, Y.; Luo, X. Cavitation detection in a Kaplan turbine based on multifractal detrended fluctuation analysis of vibration signals. *Ocean Eng.* **2022**, *263*, 112232. [CrossRef]

10.   Gohil, P.P.; Saini, R.P. Investigation into cavitation damage potentiality using pressure pulsation phenomena in a low head Francis turbine for small hydropower schemes. *Ocean Eng.* **2022**, *263*, 112230. [CrossRef]

11.   Li, D.; Zhu, Y.; Lin, S.; Gong, R.; Wang, H.; Luo, X. Cavitation effects on pressure fluctuation in pump-turbine hump region. *J. Energy Storage* **2022**, *47*, 103936. [CrossRef]

12.   Zhu, D.; Xiao, R.F.; Liu, W.C. Influence of leading-edge cavitation on impeller blade axial force in the pump mode of reversible pump-turbine. *Renew. Energy* **2021**, *163*, 939–949. [CrossRef]

13.   Hu, Z.; Cheng, Y.; Liu, D.; Chen, H.; Ji, B.; Ding, J. Broadening the operating range of pump-turbine to deep-part load by runner optimization. *Renew. Energy* **2023**, *207*, 73–88. [CrossRef]

14.   Yu, A.; Li, L.; Ji, J.; Tang, Q. Numerical study on the energy evaluation characteristics in a pump turbine based on the thermodynamic entropy theory. *Renew. Energy* **2022**, *195*, 766–779. [CrossRef]

15.   Pang, S.J.; Zhu, B.S.; Shen, Y.D.; Chen, Z.M. Study on cavitating vortex rope characteristics of reversible pump-turbine under part load turbine condition. *Phys. Fluids* **2023**, *35*, 085131. [CrossRef]

16.   Abu Shahzer, M.; Cho, Y.; Shamsuddeen, M.M.; Kim, J.H. Investigation of cavitating vortex rope instabilities and its suppression inside a Francis turbine model with Thoma number variation. *Phys. Fluids* **2023**, *35*, 033310. [CrossRef]

17.   Zhu, L.; Zhang, R.; Yu, A.; Lu, L.; Luo, X. Suppression of vortex rope oscillation and pressure vibrations in Francis turbine draft tube using various strategies. *J. Hydrodyn.* **2021**, *33*, 534–545. [CrossRef]

18.   Zhou, X.; Shi, C.; Miyagawa, K.; Wu, H. Effect of modified draft tube with inclined conical diffuser on flow instabilities in Francis turbine. *Renew. Energy* **2021**, *172*, 606–617. [CrossRef]

19.   Altimemy, M.; Attiya, B.; Daskiran, C.; Liu, I.H.; Oztekin, A. Mitigation of flow-induced pressure fluctuations in a Francis turbine operating at the design and partial load regimes—LES simulations. *Int. J. Heat Mass Transf.* **2019**, *79*, 108444. [CrossRef]

20.   Kang, W.; Zhou, L.; Wang, Z. Analysis of flow characteristics and cavitation in the vanes of a reversible pump-turbine in pump mode. *J. Energy Storage* **2023**, *68*, 107690. [CrossRef]

21.   Liu, K.; Liu, Z.; Yang, Z.; Zhang, X.; Tai, R.; Cheng, Y. Evolution and influence of pump-turbine cavitation during load rejection transients of a pumped-storage plant. *J. Hydraul. Res.* **2022**, *60*, 527–542. [CrossRef]

22.   Hidalgo, V.; Luo, X.-w.; Escaler, X.; Ji, B.; Aguinaga, A. Implicit large eddy simulation of unsteady cloud cavitation around a plane-convex hydrofoil. *J. Hydrodyn.* **2015**, *27*, 815–823. [CrossRef]

23.   Ji, B.; Long, Y.; Long, X.; Qian, Z.; Zhou, J. Large eddy simulation of turbulent attached cavitating flow with special emphasis on large scale structures of the hydrofoil wake and turbulence-cavitation interactions. *J. Hydrodyn.* **2017**, *29*, 27–39. [CrossRef]

24.   Duan, L.; Wu, X.; Ji, Z.; Fang, Q. Entropy generation analysis on cyclone separators with different exit pipe diameters and inlet dimensions. *Chem. Eng. Sci.* **2015**, *138*, 622–633. [CrossRef]

25.   Chen, H.; Lu, Y.; Liu, K.; Zhang, Z.; Li, H.; Huang, X.; Zhao, W.; Wang, Z. Study on the Internal Flow Characteristics of Long and Short Blade Runners of a 1000 MW Francis Turbine under Different Opening Conditions. *Processes* **2023**, *11*, 1796. [CrossRef]

26.   Tang, Q.; Yu, A.; Wang, Y.; Tang, Y.; Wang, Y. Numerical analysis of vorticity transport and energy dissipation of inner-blade vortex in Francis turbine. *Renew. Energy* **2023**, *203*, 634–648. [CrossRef]

27.   Zhang, F.; Fang, M.; Tao, R.; Liu, W.; Gui, Z.; Xiao, R. Investigation of energy loss patterns and pressure fluctuation Spectrum for pump-turbine in the reverse pump mode. *J. Energy Storage* **2023**, *72*, 108275. [CrossRef]

28.   Yu, Z.; Yan, Y.; Wang, W.; Liu, X. Entropy production analysis for vortex rope of a Francis turbine using hybrid RANS/LES method. *Int. Commun. Heat Mass Transfer* **2021**, *127*, 105494. [CrossRef]

29.   Xu, L.; Guo, T.; Wang, W. Effects of Vortex Structure on Hydraulic Loss in a Low Head Francis Turbine under Overall Operating Conditions Base on Entropy Production Method. *Renew. Energy* **2022**, *198*, 367–379.

30.   Wu, Y.; Zhu, D.; Tao, R.; Xiao, R.; Liu, W. Analysis of two-phase flow in cavitation condition of pump-turbine based on dynamic mode decomposition method in turbine mode. *J. Energy Storage* **2022**, *56*, 106107. [CrossRef]

31.   Zhao, Y.; Li, D.; Chang, H.; Fu, X.; Wang, H.; Qin, D. Suppression effect of bionic guide vanes with different parameters on the hump characteristics of pump-turbines based on entropy production theory. *Energy* **2023**, *283*, 128650. [CrossRef]

32.   Zhang, Y.; Jiang, W.; Qi, S.; Xu, L.; Wang, Y.; Chen, D. Clocking effect on the internal flow field and pressure fluctuation of PAT based on entropy production theory. *J. Energy Storage* **2023**, *69*, 107932. [CrossRef]

33.   Ji, L.; Xu, L.; Peng, Y.; Zhao, X.; Li, Z.; Tang, W.; Liu, D.; Liu, X. Experimental and Numerical Simulation Study on the Flow Characteristics of the Draft Tube in Francis Turbine. *Machines* **2022**, *10*, 230. [CrossRef]

34.   Sun, L.; Guo, P.; Li, Y. Experimental investigation on the characteristics and alleviation of the upper part load pressure fluctuation in a Francis turbine. *Phys. Fluids* **2023**, *35*, 064122.

35.   Kumar, S.; Cervantes, M.J.; Gandhi, B.K. Rotating vortex rope formation and mitigation in draft tube of hydro turbines—A review from experimental perspective. *Renew. Sustain. Energy Rev.* **2021**, *136*, 110354. [CrossRef]

36.   Yang, F.; Li, Z.; Cai, Y.; Jiang, D.; Tang, F.; Sun, S. Numerical Study for Flow Loss Characteristic of an Axial-Flow Pump as Turbine via Entropy Production Analysis. *Processes* **2022**, *10*, 1695. [CrossRef]

37. Qin, Y.; Li, D.; Wang, H.; Liu, Z.; Wei, X.; Wang, X. Investigation on the relationship between hydraulic loss and vortex evolution in pump mode of a pump-turbine. *J. Hydrodyn.* **2022**, *34*, 555–569. [CrossRef]
38. Deng, W.; Li, Z.; Ji, L.; Shang, L.; Liu, D.; Liu, X. Laser Doppler Velocimetry Test of Flow Characteristics in Draft Tube of Model Pump Turbine. *Processes* **2022**, *10*, 1323. [CrossRef]